2020

# Blueprinting Photothermal Shape-Morphing of Liquid Crystal Elastomers

Alexa S. Kuenstler
*University of Massachusetts Amherst*

Yuzhen Cheng
*University of California, Los Angeles*

Phuong Bui
*University of Massachusetts Amherst*

Hyunki Kim
*University of Massachusetts Amherst*

Antonio DeSimone
*SISSA-International School for Advanced Studies*

*See next page for additional authors*



Kuenstler, Alexa S.; Cheng, Yuzhen; Bui, Phuong; Kim, Hyunki; DeSimone, Antonio; Jin, Lihua; and Hayward, Ryan C., "Blueprinting Photothermal Shape-Morphing of Liquid Crystal Elastomers" (2020). *Advanced Materials*. 18.
https://doi.org/10.1002/adma.202000609

# Blueprinting Photothermal Shape-Morphing of Liquid Crystal Elastomers

*Alexa S. Kuenstler**, Yuzhen Chen**, Phuong Bui, Hyunki Kim, Antonio DeSimone*, Lihua Jin*, and Ryan C. Hayward**

A. S. Kuenstler, P. Bui, H. Kim, Prof. R. C. Hayward
Department of Polymer Science and Engineering, University of Massachusetts, Amherst, MA 01003, USA
E-mail: hayward@umass.edu

Y. Chen, Prof. L. Jin
Department of Mechanical and Aerospace Engineering, University of California, Los Angeles, CA 90095, USA
E-mail: lihuajin@seas.ucla.edu

Prof. A. DeSimone
MathLab, SISSA-International School for Advanced Studies, 34136 Trieste, Italy
Department of Excellence in Robotics and AI, Scuola Superiore Sant'Anna, Pisa, Italy
E-Mail: desimone@sissa.it

**Denotes equal contribution

Keywords: liquid crystal elastomers, photoresponsive materials, shape programming

Liquid crystal elastomers (LCEs) are an attractive platform for dynamic shape morphing due to their ability to rapidly undergo large deformations. While recent work has focused on patterning the director orientation field to achieve desired target shapes, this strategy cannot be generalized to material systems where high-resolution surface alignment is impractical. Instead of programming the local orientation of anisotropic deformation, we develop here an alternative strategy for prescribed shape morphing by programming the magnitude of stretch ratio in a thin LCE sheet with constant director orientation. By spatially patterning the concentration of gold nanoparticles (AuNPs), uniform illumination leads to gradients in photothermal heat generation and therefore spatially-nonuniform deformation profiles that drive out-of-plane buckling of planar films into predictable three-dimensional (3D) shapes. Experimentally realized shapes are shown to agree closely with both finite element simulations and geometric predictions for systems with unidirectional variation in

deformation magnitude. Finally, we demonstrate the possibility to achieve complex oscillatory motion driven by uniform illumination of a free-standing patterned sheet.

Morphing of two-dimensional sheets into three-dimensional shapes is a useful strategy to dynamically alter the physical properties of materials, offering diverse applications in fields ranging from biomedical devices to advanced manufacturing.[1] Over the past decade, numerous studies have focused on programming desired three-dimensional structures of soft materials such as shape-memory polymers (SMPs)[2,3] and gels[4–7] by introducing spatial variations in thermal expansion/contraction, swelling, or molecular order.[8] A particularly useful class of materials to achieve dynamic two-dimensional (2D) to three-dimensional (3D) shape transformations are liquid crystal elastomers (LCEs), where the coupling between the orientational ordering of polymerized mesogens and the conformation of a polymer backbone can be leveraged for large, anisotropic deformations that are dictated by the director field.[9,10] Using oriented surface alignment layers[11] or microchannels,[12] director orientation can be patterned with a resolution approaching 10 μm.[13] A subsequent reduction of nematic ordering, usually driven by heating, leads to local contraction along the director and expansion along the transverse directions, driving out-of-plane buckling into 3D shapes that are 'blueprinted' by the pattern of director orientation. However, while geometric methods allow for the deduction of the necessary in-plane director orientation field to generate a desired profile of Gaussian curvature,[14–17] there are a number of practical drawbacks to this approach. First, prescription of complex director fields requires significant processing, making high-throughput fabrication and evaluation of designs challenging. Additionally, the surface alignment methods needed to specify director orientation with high spatial resolution are only amenable to certain chemistries due to the need for high mesogen content, and thus cannot be widely generalized to all LCE systems. For example, while classical LCE systems based on siloxanes,[18,19] as well as recently developed systems that rely on simple and efficient 'click' chemistries,[20] offer attractive

thermal and mechanical properties for shape-morphing systems, they typically only allow for alignment of the director field with coarse spatial resolution such as through application of shear stress[21–23] or magnetic fields.[24] To circumvent the need for a spatially-varying director orientation, where the *direction* of deformation varies but the magnitude is constant, a potential alternative method to drive shape changes is to instead locally prescribe the *magnitude* of deformation within an otherwise homogeneous director field. While spatial variations in the extent of deformation have been widely employed for shape programming of isotropic gels,[4,7,25–28] and briefly considered in seminal theoretical work on LC polymers,[29] this approach has yet to be experimentally realized in LCE systems. Furthermore, no theory for this means of shape programming in anisotropic materials exists despite the potential generality of this method to any LCE system that can be aligned into a monodomain with a unidirectional director field.

While most LCE systems rely on uniform heating to trigger shape change, optically-driven shape morphing is an attractive approach owing to the remote deployability, spatiotemporal control, and dynamic reconfigurability offered by using light as a control stimulus. Furthermore, light-responsive systems are particularly useful for programming deformation profiles, either through spatiotemporally patterned light fields or flood illumination of materials containing localized inclusions of photothermal or photochemical moieties.[8] Programmed buckling in response to both patterned and flood illumination has been widely exploited in gel[30–32] and shape-memory polymer systems.[33–36] In contrast, work on liquid crystalline materials has focused primarily on the use of spatially patterned light[37–40] with a few exceptions including azobenzene-containing LCEs with shapes blueprinted by director orientation[41] and glassy LC polymer cantilevers with coarsely patterned photothermal hinges.[42]

Recently, we introduced a method to spatially pattern gold nanoparticles (AuNPs) in LCE fibers[43] and hydrogel sheets[44] with high spatial resolution using UV-induced photoreduction of gold salt.[45,46] Following patterning, exposure to visible light induces localized photothermal deformation that drives shape-morphing. In this work, we explore the utility of this method to blueprint shape changes of thin LCE nanocomposite (LCENC) sheets with unidirectional in-plane director fields in response to flood illumination. Specifically, we show that discrete patterns of photothermal inclusions can generate a rich array of dynamic shape changes due to buckling driven by nearly discontinuous changes of in-plane deformation. Furthermore, smooth variations in deformation can be programmed via grayscale patterning of AuNP absorbance to yield more complex shape changes. Finite element method (FEM) simulations are used to help understand the shapes selected by these materials, in concert with an analytical model based on the principles of Gaussian morphing[4,47–49] that provides a general approach to the design of axisymmetric shapes through unidirectionally varying stretch profiles.

To fabricate monodomain LCEs, 50 μm thick planar nematic films are synthesized following the work of Ahn and co-workers (see Supplementary Information, **Scheme S**1).[50] This chemistry is employed due to its amenability to formation of monodomain samples with relatively low nematic-isotropic transition temperatures ($T_{NI}$) and large thermomechanical strains. Briefly, n-dodecylamine and 8-amino-1-octanol are mixed in a 1:1 molar ratio with the diacrylate mesogen RM82 with an overall stoichiometry of acrylate:amine functionalities of 1.1:1, selected to afford a cross-link density that allows for large strains while maintaining sufficient mechanical robustness. All reactants are melted in a vial with 1 wt% photoinitiator, filled between two rubbed polyimide-coated glass slides, and oligomerized in an oven overnight at 55°C. Following oligomerization, films are photopolymerized under UV light and the resulting monodomain samples harvested. To impart photo-responsiveness, gold nanoparticles (AuNPs) are produced by in-situ photoreduction of gold salt within the pre-formed LCE films

as previously reported.[43] LCE samples are swollen with a solution of $HAuCl_3$, oleylamine, and photoinitiator and exposed to UV light through a photomask to produce AuNPs via photochemical reduction (**Figure 1**A). Because the degree of gold reduction is controlled by the dose of UV light, the resulting absorbance of the nanocomposite can be spatially programmed using grayscale photomasks (**Figure 1**B).[26]

The as-synthesized films are monodomain with a constant director orientation (**Figure S**1) with an order parameter of S ≈ 0.6 as measured by wide-angle X-ray scattering (WAXS),[51] with a glass transition temperature of $T_g \approx$ -4 °C, a broad $T_{NI} \approx$ 100 °C, and an elastic modulus parallel to the director of E ≈ 9 MPa (**Figure S**2). We note that introduction of AuNPs does not significantly affect the thermal or mechanical properties of the films, as evidenced by DSC, TGA, and tensile tests (**Figure S**2). Upon uniformly heating above 40 °C, samples reversibly contract along the director and expand in the perpendicular directions, ultimately contracting to 60% of their initial length along the director when heated to 120 °C (**Figure 1**C). To probe the effect of photothermal heat generation on deformation, films are placed on a hot plate at a defined temperature and exposed to 200 mW $cm^{-2}$ of light with wavelength 530 nm. The length at each temperature is recorded to define a stretch ratio, $\lambda = l_{final}/l_{initial}$ where $l_{initial}$ is defined as the length along the director at room temperature. As shown in **Figure 1**C for the case of maximum light absorbance, a photo-induced temperature change of ΔT ≈ 20 °C (**Figure S**3) is observed. We note that in principle this temperature change could be substantially greater and is limited by the intensity of the incident light source. Photo-deformation is maximized when samples are held at 80-90 °C due to the proximity to $T_{NI}$; thus, all subsequent experiments are conducted at an ambient temperature of 85°C. Because AuNP absorbance determines the magnitude of temperature change upon photothermal heating, control of light dose during photoreduction can be used to systematically program the resulting photo-deformation. As

shown in **Figure 1**D, the stretch $\lambda$ due to photothermal heating can be programmed from 0.77 – 0.92 by controlling the transparency of the photomask to UV light from 0% black (nearly transparent to UV light) and 100% black (nearly opaque) during patterning. This introduces the possibility to locally control photo-deformation—and thus shape transformation—through judicious design of photomasks.

To connect the patterned photothermal heat generation to shape transformation, we develop FEM simulations and a geometric model. In the FEM simulations, LCE sheets are modeled using the neo-classical free energy density[52,53] implemented into Abaqus as a user subroutine UMAT. A stretch-temperature relation, fit to the experimental measurement (**Figure 1**C), is introduced into the free energy to describe the temperature-dependent anisotropy of LCEs (see **Experimental Section** and **Supporting Information**). Once a temperature field corresponding to a specific design of photothermal patterning is prescribed, the equilibrium shape is solved by FEM in Abaqus.

To model these shape changes geometrically, we turn to the principle of Gaussian morphing,[48,49] previously exploited for isotropic systems, and apply it to the anisotropic case considered here. In this model, the in-plane deformation due to photothermal heat generation defines a 'target metric' that describes how the distance between points in the flat sheet should change upon deployment to generate a shape of defined curvature. We consider the case of sheets with uniform orientation of the director along the *u* axis (**Figure 1**A), where the magnitude of stretch $\lambda$ is constant along *u* and varies as a function of *v*. Thus, the metric tensor is given by

$$\boldsymbol{g} = \begin{bmatrix} \lambda^2(v) & 0 \\ 0 & \frac{1}{\lambda(v)} \end{bmatrix} \quad (1)$$

Crucially, in this case, the local magnitude of stretch varies while the direction is constant, similar to the case of isotropic gels[4,7,25–28] and equibiaxially-strained thermoplastics[35,54] but distinct from the case of a director field with patterned orientation but uniform magnitude of stretch.[11,17] Using Gauss's *theorema egregium* (see **Supplementary Information** for a more detailed discussion), the Gaussian curvature can be calculated from the metric tensor by

$$K = -\frac{1}{\sqrt{\lambda}}\left(\sqrt{\lambda}\lambda'\right)' = -\frac{2}{3\sqrt{\lambda}}\left(\lambda^{3/2}\right)'' \quad (2)$$

Thus, by solving Equation 2 for a desired curvature profile $K(v)$, a corresponding stretch profile $\lambda(v)$ can be computed. Finally, using an experimentally-determined calibration curve of stretch vs grayscale, a photomask can be generated to pattern the necessary photothermal profile is patterned into the nematic sheets (see **Supporting Information** for additional detail).

Using this patterning method, we first investigate the effect of discretely patterned deformation profiles on the buckling of nematic sheets using a bi-strip geometry, where one-half of a square sheet is patterned with a stripe of AuNPs such that the photoactive region bisects the length of the sheet with the long axis of the stripe parallel to the director (**Figure 1**A). For the case where the lateral dimensions of the square film are much greater than the thickness (here, width/thickness = 200), heat dissipation by convection limits thermal broadening across the interface between the photoactive and non-photoactive regions (**Figure S**3B and **Supporting Information**). In addition, despite a through-thickness gradient in heat generation due to the strong absorption of light by the nanoparticles that is necessary to generate appreciable temperature changes, the thin nature of these films ensures that the resulting temperature distribution is nearly constant through the thickness of the film (**Figure S**3C). For the simple case of a discrete photothermally-heated stripe, the equilibrium in-plane length is almost discontinuous across the stripe interface as the photoactive region contracts along the director and the energetic cost of this step-change in deformation is relieved by buckling out-of-plane.

For square films with side length $l$ = 10 mm, the films preferentially roll about an axis perpendicular to the photothermal interface to form a bottleneck shape upon illumination as shown in **Figure 1**E, where the non-heated and heated regions adopt different radii of curvature that are smoothly connected over the interfacial region as predicted by FEM. We note that films tend to roll with the direction of curvature away from the light. This suggests that while small asymmetries in heating through the thickness inevitably exist due to the decay in light intensity, this is not the dominant factor in biasing the buckling direction of the film, since a higher temperature at the surface of the film facing the incident light should prefer curvature toward the light source. This shape transformation is analogous to the case of isotropic hydrogel bi-strips with two discrete regions of cross-link density.[55] This shape transformation can be rationalized as follows: while a discontinuous target metric encodes divergent positive and negative Gaussian curvature on either side of the interface, the non-zero thickness of a real sheet, and the corresponding bending energy cost to deform it, causes the curvature to be smoothed out across the interface into regions of finite Gaussian curvature with opposite signs. The resulting shape consists of two zero-$K$ regions on either end of the sheet, smoothly connected by a neck that contains regions of both positive and negative Gaussian curvature, wherein stretching energy (i.e. deviations from the discontinuous target metric) balances the overall bending energy of the sheet.

To probe the utility of this method to program a wider variety of shapes, a series of additional patterns are investigated. For example, illumination of a square sheet with a centered rectangular inclusion with the long axis oriented parallel to the director results in a saddle-like shape that is symmetric about the axes parallel and perpendicular to the director that bisect the center of the film (**Figure 2**A). Placement of a photothermal region in one quadrant of the film drives bending about an axis diagonally bisecting the sheet, resulting in a wrinkled hyperbolic surface (**Figure 2**B). Finally, inclusion of a large square in the center of the sheet drives rolling

about an axis perpendicular to the director and wrinkling along the edges of the sheet (**Figure 2**C). These deformations are similar to those observed in nematic sheets with polydomain inclusions[56] and isotropic gels with local photothermal inclusions[44] and again result from a balance of stretching and bending energies as the films attempt to accommodate the discontinuous target metric.

Remarkably, a simple change in the direction of the film edges with respect to the director and photothermal inclusions leads to more complex behavior. When nanoparticles are patterned in half of the film with the interface between the photoactive and non-photoactive region extending diagonally between opposing corners of a square film at a 45° angle to the director (**Figure 2**D), flood illumination from directly above the film drives wrinkling as observed for the other striped case (**Figure S**4). However, when the sheet is illuminated from a 30° angle with respect to the substrate along the edge parallel to the director, the film is observed to oscillate continuously between two buckling modes (**Figure 2**E-G, **Videos S1-2**, and **Supporting Information**). Initially, the film adopts a geometry such that the edge of the film along the director curls about an axis perpendicular to the director, denoted as Mode 1. However, the shape slowly evolves over a few seconds to become a full wavelength wrinkle (Mode 2) that quickly snaps back to Mode 1 after several seconds as evidenced by the nearly discontinuous change in film edge displacement when tracked from a 60 fps video (**Figure 2**F), with a characteristic snapping time of ≈ 0.1 s. This cycle then repeats for the duration of illumination. Inter-snap times range from 1.2 to 11.8 seconds, with an average time of 3.8 seconds. While oscillation due to self-shadowing effects[37,42,57–59] and snapping between two bistable shapes[60,61] has been reported previously in nematic beams, cyclic oscillation via photoinduced snapping has only been reported in one other case,[62] to our knowledge. We hypothesize that this phenomenon is driven by self-shadowing, where slight changes in the incident light intensity due to deformation toggles the equilibrium between buckling modes.

Though our FEM methods are unable to capture dynamic behavior at this time, we find that if a strain profile is imposed that is consistent with a high light intensity on the edge of the film and with less stretch in areas where the light would be blocked during shape evolution, Mode 2 is predicted, suggesting that self-shadowing is capable of driving a transition in buckled geometry, and hence the oscillatory snapping behavior observed here (See **Figure S**5, **Supplementary Information** for more detail). Films of other geometries do not demonstrate oscillatory behavior when exposed to similar oblique illumination conditions (**Figure S**6). While further study is warranted to fully understand the underlying mechanics of this phenomenon, this behavior suggests that localized deformation can be leveraged for non-equilibrium behavior and impulsive motion upon judicious design of photo-induced buckling instabilities and illumination conditions.

Next, we explore the utility of smoothly-varying spatial gradients in absorption to introduce continuous in-plane stretch profiles into nematic sheets, which provides opportunities to program shapes with arbitrary Gaussian curvatures. As a proof-of-concept, we first investigate the 'forward' problem, i.e. defining a stretch profile and evaluating the match between experiments, FEM simulations, and geometric predictions for the resulting 3D shape. As a convenient test case, we use stretch profiles of the following form to program square sheets:

$$\lambda(\xi) = \lambda_{min} + (\lambda_{max} - \lambda_{min})\exp\left(-\frac{1}{2}\left(\frac{2\xi-1}{d}\right)^2\right), \quad (3)$$

where $\xi = \frac{v}{w} \in [0,1]$, $\lambda_{min}$ and $\lambda_{max}$ are the minimum and maximum experimentally accessible stretches, respectively, and $d$ is a dimensionless parameter that controls the spatial extent of variations in $\lambda$ (**Figure 3**A). Indeed, as predicted by **Equation** (2), as $d$ is reduced, the resulting curvature increases in magnitude and becomes concentrated in a smaller region. Using the corresponding metric tensor, given by **Equation** (1), theory and FEM (**Figure 3**B-D) predict buckling into candy wrapper-like shapes, with a ridge of positive Gaussian curvature

in the middle of the sheet that smoothly progresses along *v* to valley regions of negative Gaussian curvature that evolve to zero Gaussian curvature at the edges. To investigate these shape transformations experimentally, samples are patterned using photomasks generated in Matlab from a calibration curve of stretch versus percent black (see **Supplementary Information** for photomasks and additional details). Experimental results (**Figure 3**E, **Figure S**7) match the predicted deformations, with greater curvature and a tighter characteristic radius of curvature of the ridge as *d* decreases. We find that the Gaussian curvatures observed by FEM (**Figure 3**B) are in very good agreement with the ones predicted by **Equation** (2), and furthermore that the realized 3D shapes correspond closely to those from geometric predictions (see (**Figure 3**C) and **Supporting Information)**. This striking agreement demonstrates the robustness of the shape morphing concept developed here and suggests its potential for generalization to other chemistries and materials.

To truly program shape transformation, the inverse problem – i.e., computing the stretch profile $\lambda(v)$ that leads to a desired 3D shape upon actuation – needs to be solved. While the corresponding differential geometry has been developed for isotropic gels with differential swelling[4,5,47] and nematic sheets with varying director orientation,[14,17] we are not aware of previous solutions for the anisotropic case of varying stretch magnitude with a homogenous director orientation. As a first step, we focus here on shapes with constant negative and positive Gaussian curvature, with the appropriate stretch functions obtained by numerically solving **Equation** (2) within the constraint of the stretches achievable in our system and constructing a polynomial fit to the solution (see **Supporting Information** and **Figure S**8 for details). The target negative and positive curvature, calculated stretch profiles, and simulated curvature generated by FEM are shown in **Figure 4**A, D. The calculated stretch profiles prescribe high deformation in the center of the sheet and low deformation at the edges parallel to the director field in the case of constant negative Gaussian curvature and the opposite – low deformation in

the middle and high deformation at the edges – for the case of constant positive Gaussian curvature. The simulated curvatures from FEM match the target constant curvatures quite well in the center portions of the films but deviate at the edges, presumably reflecting an elastic 'boundary layer'[63] that lowers the bending energy for a non-zero thickness sheet. The corresponding samples are prepared using photomasks generated from the calculated stretch profiles (see **Supplementary Information**) and experiments show buckling of LCE sheets into a saddle-like shape and a shallow spherical cap-like shape for negative and positive Gaussian curvature, respectively, matching the predictions of the accompanying FEM simulations and geometric models (**Figure 4**B-C, E-F and **Figure S**9). Interestingly, FEM predicts that a non-axisymmetric saddle shape should be lower energy than the observed axisymmetric shape in the case of constant negative Gaussian curvature (**Figure S**10). However, the non-axisymmetric shape is not observed experimentally, possibly due to imperfections in sample fabrication or kinetic selection of the axisymmetric shape. We note that the observed shapes are analogous to those experimentally realized in LCEs with patterned axisymmetric director fields about a +1 defect.[16]

In summary, we have demonstrated a method combining experiments, FEM simulations, and geometric predictions to program photoactive shape morphing from monodomain LCE sheets with a unidirectional director by spatially controlling photothermal heat generation. Discontinuous metrics introduced via localized photothermal inclusions are shown to drive buckling into both static shapes and autonomously oscillating forms. Furthermore, we developed a new theory based on Gaussian morphing to encode smoothly-varying stretch profiles to rationally approach the design of targeted shapes. We anticipate that this fabrication method is generalizable to a variety of chemistries that are incompatible with methods to spatially pattern in-plane director fields, opening up new opportunities for shape morphing in a variety of liquid crystalline polymer materials.

**Experimental Section**

*Materials*: 1,4-Bis[4-(6-acryloyloxyhexyloxy)benzoyloxy]-2-methylbenzene (RM82) was purchased from Synthon Chemicals and used as received. 8-amino-1-octanol and *n*-dodecylamine were purchased from Tokyo Chemical Industries. 2,2-dimethoxy-2-phenyl-acetophenone (Irgacure 651), oleylamine, and gold(III) chloride trihydrate ($HAuCl_4$) were purchased from Sigma Aldrich.

*LCE Fabrication*: The procedure of Ahn and co-workers[50] was followed with slight modification. RM82, dodecylamine, and 8-amino-1-octanol were combined in a molar ratio of 1.1:0.5:0.5 with 2.5 wt% of Irgacure 651 in a vial and melted at ≈ 85 °C and vortexed repeatedly. Following evacuation to remove air bubbles, the molten mixture was infiltrated via capillary action into alignment cells composed of two glass slides coated with Elvamide polyimide (DuPont), rubbed with a velvet cloth, and set to 50 μm thickness with glass spacers. Samples were placed in an oven at 55 °C to oligomerize overnight, subsequently cured with UV light (10 mW $cm^{-2}$) for 30 min and harvested by soaking in warm water and gently opening the alignment cells with a razor blade.

*Photopatterning of Nanocomposites*: Stock solutions of $HAuCl_4$ (11.8 mg, 0.035 mmol) in acetone (0.3 mL), oleylamine (59 mg, 0.22 mmol) in toluene (0.5 mL), and Irgacure 651 (56.2 mg, 0.22 mmol) in toluene (0.5 mL) were freshly prepared. To prepare the gold nanoparticle precursor solution, 200 μL of $HAuCl_4$, 400 μL of Irgacure 651, and 200 μL of oleylamine stock solutions were sequentially added to a vial and diluted with 800 μL of toluene. Films were swelled in gold solution, blotted on filter paper to remove excess solution, and sandwiched between a glass slide and a photomask. Photomasks were prepared in Matlab and Adobe Illustrator, fabricated via inkjet printing (HP LaserJet 500) on plastic transparency films (Apollo

Laser Printer Transparency Film), and glued on glass coverslips. Samples were exposed to 30 mW $cm^{-2}$ of light with 365 nm wavelength (Thorlabs) for 10 s, developed in acetone for 60 min to remove unreacted gold salt, and dried.

*Instruments and Measurement:* UV-vis spectra were recorded on a fiber optic spectrometer (Ocean Optics Flame). To evaluate photoactuation, samples were placed on a hot plate covered with filter paper to prevent sticking and heated to 85 °C. All actuation experiments were performed with a 530 nm LED (LEDSupply) generating an intensity of 200 mW $cm^{-2}$ and shape transformations were recorded using a camera (Nikon 5500). Displacement data during oscillation was extracted from recorded videos recorded at 60 fps using Tracker software (Open Source Physics). Because the time-scale of snapping is similar to that of the frame rate, blurring of images prevented the use of some frames for tracking analysis during snapping.

*FEM Simulations*

In the finite element simulations, thin LCE sheets are modeled with the same geometry as that in the experiments, i.e. a square shape with a width-to-thickness ratio of 200. We model these LCE sheets by using the neo-classical free energy density[52,53] implemented into Abaqus as a user subroutine UMAT (see **Supporting Information** for details). The ratio of the bulk modulus to the shear modulus $K/\mu$ is set as 500, which indicates that the Poisson's ratio is 0.499 and thus the sheets are nearly incompressible. A stretch-temperature relation (**Figure 1**C), fitted to the experimental measurement, is introduced into the free energy to describe the temperature-dependent anisotropy of LCEs (see **Supporting Information)**

$$\lambda = 0.6\sqrt{1 + 1.778\frac{120-T}{60}}, 60℃ \leq T \leq 120℃.$$

Although in experiments the stretch is defined with respect to the length at room temperature, in FEM simulations the lengths below 60 °C and above 120 °C are treated as those at 60 °C and

120 °C, respectively, because the difference is negligible. The above stretch-temperature relation indicates that the nematic LCEs start to deform at 60℃ and continuously deform until 120℃, yielding a maximum stretch of 0.6 parallel to the director. Using the above equation, the stretch patterns in the experiments are converted into temperature distributions, which are assigned to the LCE sheets as predefined fields. The element type is three-dimensional hybrid quadratic brick with reduced integration (Abaqus type C3D20RH). We performed a mesh refinement study to ensure that there are at least three elements along the thickness and that the aspect ratio of a single element is no greater than 5. As a result, approximately $3x10^4$ elements are involved in each finite element model. The LCE sheets in all the simulations have free boundary conditions, except the case shown in **Figure 4**B, in which symmetric boundary conditions about $u/w = 0.5$ is applied. Artificial damping is introduced into the static general procedure such that the sheets can snap to a stable equilibrium state when loss of stability occurs. The damping factor in the simulations is determined based on the dissipated energy fraction, which is set as $1x10^{-5}$, a value that can suppress instabilities without having a significant effect on the solutions.

## Supporting Information

Supporting Information is available from the Wiley Online Library or from the authors.

## Acknowledgements

A.S.K and Y.C contributed equally to this work. Support for this work was provided by the Office of Naval Research through the MURI on Photomechanical Materials (ONR N00014-18-1-2624), National Science Foundation through Grant No. CMMI 1925790, and European Research Council through Advanced Grant 340685-MicroMotility. The authors thank Daria Atkinson for helpful discussions.

Received: ((will be filled in by the editorial staff))
Revised: ((will be filled in by the editorial staff))
Published online: ((will be filled in by the editorial staff))

## References

[1] Y. Liu, J. Genzer, M. D. Dickey, *Prog. Polym. Sci.* **2016**, *52*, 79.
[2] Q. Zhao, H. J. Qi, T. Xie, *Prog. Polym. Sci.* **2015**, *49–50*, 79.
[3] A. Lendlein, O. E. C. Gould, *Nat. Rev. Mater.* **2019**, *4*, 116.
[4] Y. Klein, E. Efrati, E. Sharon, *Science* **2007**, *315*, 1116.
[5] J. Kim, J. a. Hanna, M. Byun, C. D. Santangelo, R. C. Hayward, *Science (80-. ).* **2012**, *335*, 1201.
[6] A. Sydney Gladman, E. A. Matsumoto, R. G. Nuzzo, L. Mahadevan, J. A. Lewis, *Nat. Mater.* **2016**, *15*, 413.
[7] S. J. Jeon, A. W. Hauser, R. C. Hayward, *Acc. Chem. Res.* **2017**, *50*, 161.
[8] A. S. Kuenstler, R. C. Hayward, *Curr. Opin. Colloid Interface Sci.* **2019**, *40*, 70.
[9] T. J. White, D. J. Broer, *Nat. Mater.* **2015**, *14*, 1087.
[10] R. S. Kularatne, H. Kim, J. M. Boothby, T. H. Ware, *J. Polym. Sci. Part B Polym. Phys.* **2017**, *55*, 395.
[11] T. H. Ware, M. E. McConney, J. J. Wie, V. P. Tondiglia, T. J. White, *Science (80-. ).* **2015**, *347*, 982.
[12] Y. Xia, G. Cedillo-Servin, R. D. Kamien, S. Yang, *Adv. Mater.* **2016**, *28*, 9637.
[13] B. A. Kowalski, V. P. Tondiglia, T. Guin, T. J. White, *Soft Matter* **2017**, *13*, 4335.
[14] H. Aharoni, E. Sharon, R. Kupferman, *Phys. Rev. Lett.* **2014**, *113*, 257801.
[15] P. Plucinsky, B. A. Kowalski, T. J. White, K. Bhattacharya, *Soft Matter* **2018**, *14*, 3127.
[16] B. A. Kowalski, C. Mostajeran, N. P. Godman, M. Warner, T. J. White, *Phys. Rev. E* **2018**, *97*, 1.
[17] H. Aharoni, Y. Xia, X. Zhang, R. D. Kamien, S. Yang, *Proc. Natl. Acad. Sci.* **2018**, *115*, 7206.
[18] Jürgen Küpfer, Jürgen Küpfer, H. Finkelmann, H. Finkelmann, *Die Makromol. Chemie, Rapid Commun.* **1991**, *12*, 717.
[19] H. Wermter, H. Finkelmann, *e-Polymers* **2001**, *1*, 111.
[20] M. O. Saed, A. H. Torbati, C. A. Starr, R. Visvanathan, N. A. Clark, C. M. Yakacki, *J. Polym. Sci. Part B Polym. Phys.* **2017**, *55*, 157.
[21] C. M. Yakacki, M. Saed, D. P. Nair, T. Gong, S. M. Reed, C. N. Bowman, *RSC Adv.* **2015**, *5*, 18997.
[22] A. Kotikian, R. L. Truby, J. W. Boley, T. J. White, J. A. Lewis, *Adv. Mater.* **2018**, *30*, 1.
[23] M. O. Saed, C. P. Ambulo, H. Kim, R. De, V. Raval, K. Searles, D. A. Siddiqui, J. M. O. Cue, M. C. Stefan, M. R. Shankar, T. H. Ware, *Adv. Funct. Mater.* **2019**, *29*, 1.
[24] Y. Yao, J. T. Waters, A. V. Shneidman, J. Cui, X. Wang, N. K. Mandsberg, S. Li, A. C. Balazs, J. Aizenberg, *Proc. Natl. Acad. Sci.* **2018**, *115*, 12950.
[25] Z. L. Wu, M. Moshe, J. Greener, H. Therien-Aubin, Z. Nie, E. Sharon, E. Kumacheva, *Nat. Commun.* **2013**, *4*, 1.
[26] J. H. Na, N. P. Bende, J. Bae, C. D. Santangelo, R. C. Hayward, *Soft Matter* **2016**, *12*, 4985.
[27] H. Thérien-Aubin, M. Moshe, E. Sharon, E. Kumacheva, *Soft Matter* **2015**, *11*, 4600.
[28] L. Huang, R. Jiang, J. Wu, J. Song, H. Bai, B. Li, Q. Zhao, T. Xie, *Adv. Mater.* **2017**, *29*, 1.

[29] C. D. Modes, K. Bhattacharya, M. Warner, *Proc. R. Soc. A Math. Phys. Eng. Sci.* **2011**, *467*, 1121.
[30] Z. Zhu, E. Senses, P. Akcora, S. A. Sukhishvili, *ACS Nano* **2012**, *6*, 3152.
[31] E. Wang, M. S. Desai, S. W. Lee, *Nano Lett.* **2013**, *13*, 2826.
[32] A. W. Hauser, A. A. Evans, J. H. Na, R. C. Hayward, *Angew. Chemie - Int. Ed.* **2015**, *54*, 5434.
[33] Y. Liu, J. K. Boyles, J. Genzer, M. D. Dickey, *Soft Matter* **2012**, *8*, 1764.
[34] Y. Liu, B. Shaw, M. D. Dickey, J. Genzer, *Sci. Adv.* **2017**, *3*, e1602417.
[35] A. M. Hubbard, R. W. Mailen, M. A. Zikry, M. D. Dickey, J. Genzer, *Soft Matter* **2017**, *13*, 2299.
[36] T. F. Scott, A. D. Schneider, W. D. Cook, C. N. Bowman, *Science (80-. ).* **2005**, *308*, 1615.
[37] A. W. Hauser, D. Liu, K. C. Bryson, R. C. Hayward, D. J. Broer, *Macromolecules* **2016**, *49*, 1575.
[38] M. Lahikainen, H. Zeng, A. Priimagi, *Nat. Commun.* **2018**, *9*, 4148.
[39] J.-A. Lv, Y. Liu, J. Wei, E. Chen, L. Qin, Y. Yu, *Nature* **2016**, *537*, 179.
[40] M. K. McBride, M. Hendrikx, D. Liu, B. T. Worrell, D. J. Broer, C. N. Bowman, *Adv. Mater.* **2017**, *29*, 1606509.
[41] S. K. Ahn, T. H. Ware, K. M. Lee, V. P. Tondiglia, T. J. White, *Adv. Funct. Mater.* **2016**, *26*, 5819.
[42] A. H. Gelebart, G. Vantomme, E. W. Meijer, D. J. Broer, *Adv. Mater.* **2017**, *29*, 1606712.
[43] A. S. Kuenstler, H. Kim, R. C. Hayward, *Adv. Mater.* **2019**, *31*, 1901216.
[44] H. Kim, J. Kang, Y. Zhou, A. S. Kuenstler, Y. Kim, C. Chen, T. Emrick, R. C. Hayward, *Adv. Mater.* **2019**, *31*, 1900932.
[45] M. L. Marin, K. L. Mcgilvray, J. C. Scaiano, *J. Am. Chem. Soc.* **2008**, 16572.
[46] A. S. Korchev, M. J. Bozack, B. L. Slaten, G. Mills, *J. Am. Chem. Soc.* **2004**, *126*, 10.
[47] E. Sharon, E. Efrati, *Soft Matter* **2010**, *6*, 5693.
[48] M. Arroyo, A. Desimone, *J. Mech. Phys. Solids* **2014**, *62*, 99.
[49] G. Cicconofri, M. Arroyo, G. Noselli, A. DeSimone, *Int. J. Non. Linear. Mech.* **2020**, *118*, 103278.
[50] H. H. Yoon, D. Y. Kim, K. U. Jeong, S. K. Ahn, *Macromolecules* **2018**, *51*, 1141.
[51] M. Deutsch, *Phys. Rev. A* **1991**, *44*, 8264.
[52] L. Jin, Z. Zeng, Y. Huo, *J. Mech. Phys. Solids* **2010**, *58*, 1907.
[53] P. Bladon, M. Terentjev, M. Warner, *Phys. Rev. E* **1993**, *47*, 3838.
[54] R. W. Mailen, C. H. Wagner, R. S. Bang, M. Zikry, M. D. Dickey, J. Genzer, *Smart Mater. Struct.* **2019**, *28*, 045011.
[55] J. Kim, J. A. Hanna, R. C. Hayward, C. D. Santangelo, *Soft Matter* **2012**, *8*, 2375.
[56] C. Ahn, X. Liang, S. Cai, *Extrem. Mech. Lett.* **2015**, *5*, 30.
[57] T. J. White, N. V. Tabiryan, S. V. Serak, U. A. Hrozhyk, V. P. Tondiglia, H. Koerner, R. A. Vaia, T. J. Bunning, *Soft Matter* **2008**, *4*, 1796.
[58] K. M. Lee, M. L. Smith, H. Koerner, N. Tabiryan, R. A. Vaia, T. J. Bunning, T. J. White, *Adv. Funct. Mater.* **2011**, *21*, 2913.
[59] A. H. Gelebart, D. Jan Mulder, M. Varga, A. Konya, G. Vantomme, E. W. Meijer, R. L. B. Selinger, D. J. Broer, *Nature* **2017**, *546*, 632.
[60] M. R. Shankar, M. L. Smith, V. P. Tondiglia, K. M. Lee, M. E. McConney, D. H. Wang, L. S. Tan, T. J. White, *Proc. Natl. Acad. Sci. U. S. A.* **2013**, *110*, 18792.
[61] A. A. Skandani, S. Chatterjee, M. L. Smith, J. Baranski, D. H. Wang, L. S. Tan, T. J. White, M. R. Shankar, *Extrem. Mech. Lett.* **2016**, *9*, 45.
[62] H. Zeng, M. Lahikainen, L. Liu, Z. Ahmed, O. M. Wani, M. Wang, H. Yang, A. Priimagi, *Nat. Commun.* **2019**, *10*, 1.

[63] E. Efrati, E. Sharon, R. Kupferman, *Phys. Rev. E* **2009**, *80*, 1.

## Figures

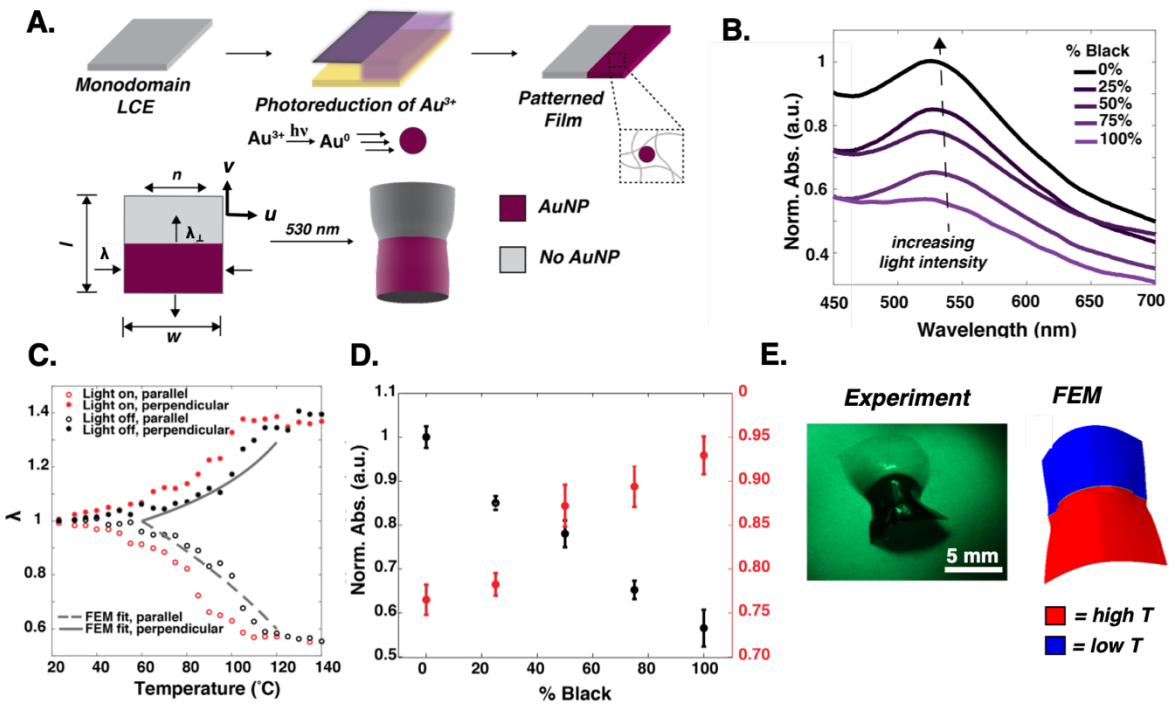


**Figure 1**. **Photopatterning and photothermal properties of LCENCs**. (**A**) AuNPs are spatially incorporated into LCEs via photoreduction of gold salt with UV light. Upon illumination with visible light, local heating induces a contraction along the director and buckling into a prescribed shape. (**B**) AuNP absorbance is controlled by modulating the light dose via grayscale photomasks that vary from 0% black (transparent) to 100% black (opaque). (**C**) Stretch vs temperature with (red) and without (black) photothermal heating for the case of highest absorbance. Because of the high $T_{NI}$ of these materials experiments are performed at 85 °C to maximize photo-deformation. (**D**) Absorbance and stretch as functions of the opacity of the photomasks. Stretch can be spatially programmed over a range of 20%. (**E**) Example of a sheet programmed with a bi-strip geometry. Contraction along the director parallel to the interface between photothermally-heated and non-heated regions results in rolling about an axis perpendicular to this interface.

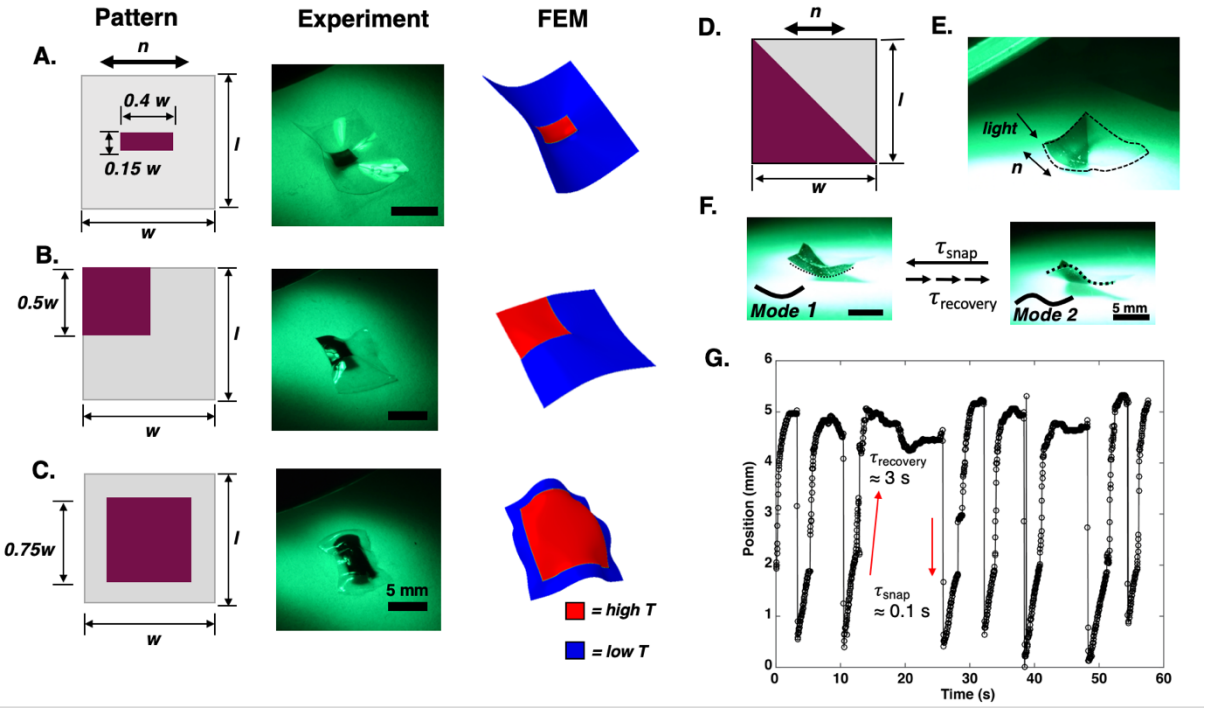


**Figure 2. Shape transformation via localized photothermal inclusions**. Buckling into different shapes in response to (**A**) rectangular and (**B**, **C**) square inclusion are demonstrated experimentally and the resulting shapes are predicted via FEM. **(D**, **E)** A square film is patterned with the photothermal region bisecting the film at 45° with respect to the director with incident light on the corner of the photothermal region. **(F)** The film snaps between a half wavelength to a full wavelength wrinkle reversibly. Upon relaxing to the initial state, the process repeats. **(G)** Position of the edge of the film with respect to the substrate vs time. The film gradually evolves over a few seconds to Mode 2 before snapping through to Mode 1 in ≈ 0.1 s. The film exhibits mechanical bistability between the two modes and autonomously oscillates between them for the duration of illumination.

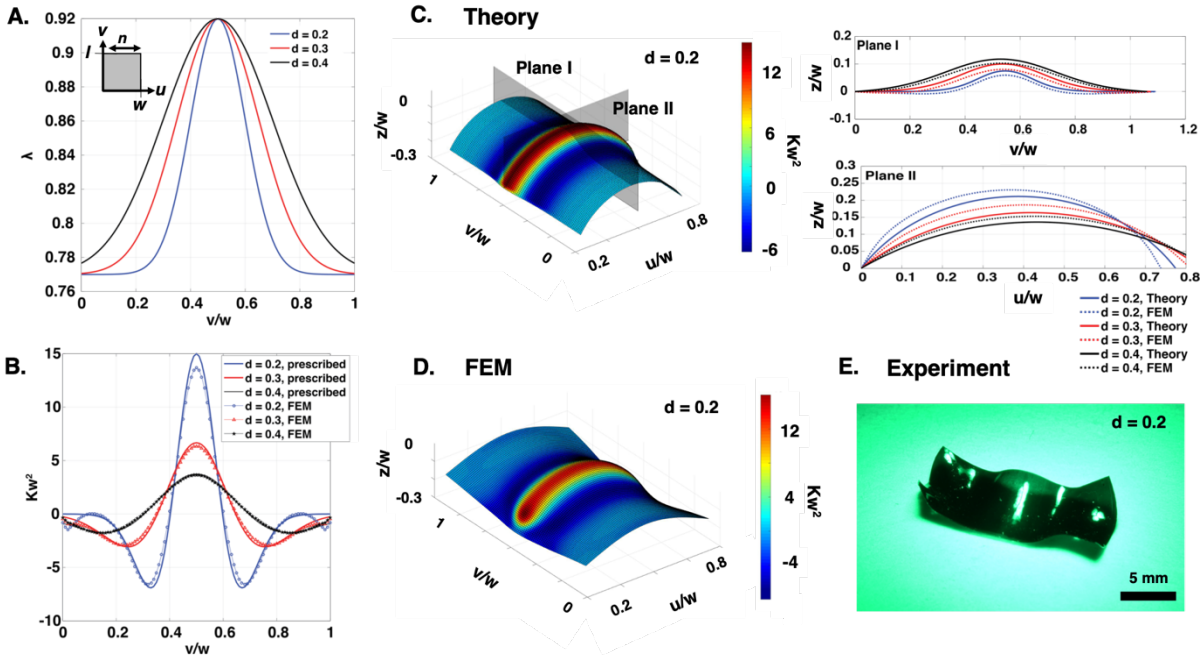


**Figure 3. Patterning smoothly curved sheets with Gaussian stretch profiles. (A)** Stretch profiles $\lambda$ for different values of $d$ for $w = l$ (inset). **(B)** Prescribed and FEM Gaussian curvature as a function of $v$ at $u/w = 0.5$. **(C)** Shape prediction of $d = 0.2$ by theory (left) and comparison of theory to FEM simulations (right) for different values of $d$. **(D)** Shape prediction of $d = 0.2$ by FEM. **(E)** Experimental result for $d = 0.2$ demonstrates buckling into a candy wrapper-like shape due to regions of highly localized Gaussian curvature that closely matches the predicted shape by theory and FEM. Results for $d = 0.3$ and 0.4 are provided in the Supporting Information.

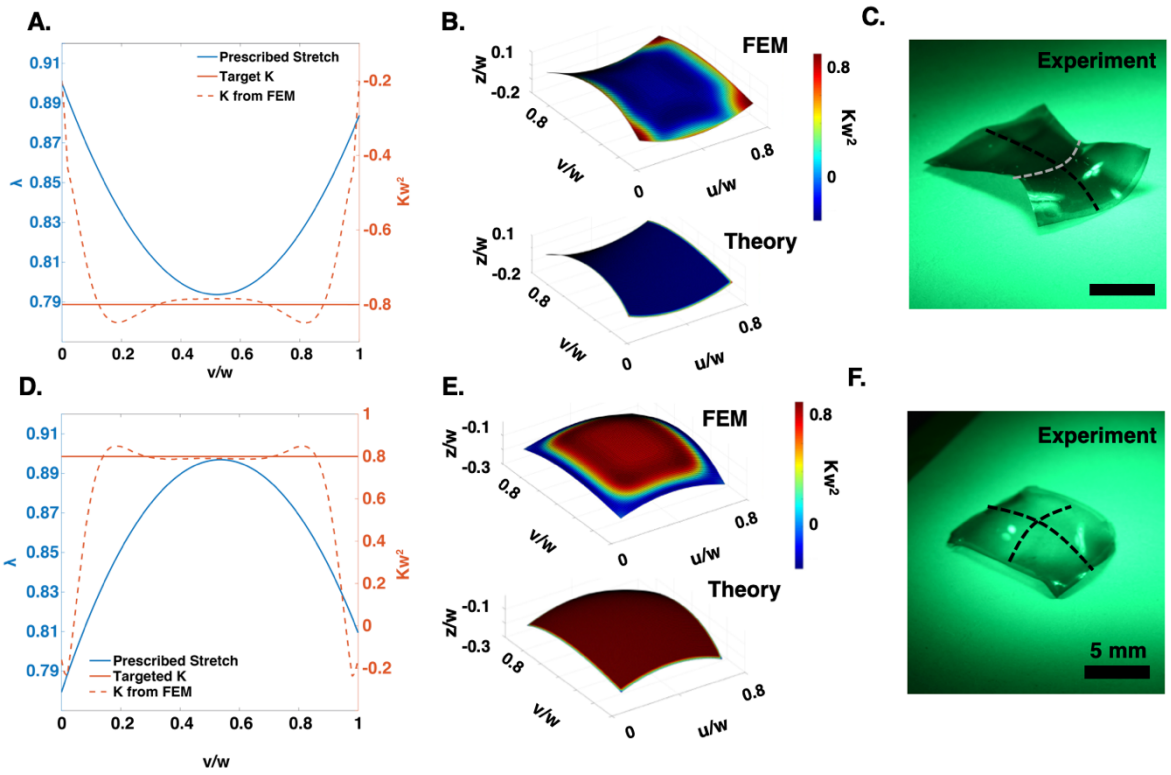


**Figure 4. Programmed constant negative and positive Gaussian curvature via ninth-order polynomial stretch profiles. (A)** Prescribed and predicted Gaussian curvature, **(B)** FEM simulation (top) and theory (bottom) and **(C)** experiment for negative Gaussian curvature. **(D)** Prescribed and predicted Gaussian curvature, **(E)** FEM simulation and **(F)** experiment for positive Gaussian curvature. White and black lines are drawn as guides to the eyes, with black and white denoting positive and negative curvature, respectively.

Light-driven shape morphing via spatially-patterned photothermal deformation of liquid crystal elastomers is demonstrated. Distinct from shape prescription via modulation of the director orientation, a general method for patterning deformation profiles in monodomain elastomers with a unidirectional director field is presented. A model for prescribing Gaussian curvature via continuous deformation profiles is presented and validated with experiments and finite element analysis.

**Keyword** photoactive materials

*Alexa S. Kuenstler**, Yuzhen Chen**, Phuong Bui, Hyunki Kim, Antonio DeSimone*, Lihua Jin*, and Ryan C. Hayward**

**Title** Blueprinting Photothermal Shape-Morphing of Liquid Crystal Elastomers

ToC figure ((Please choose one size: 55 mm broad × 50 mm high or 110 mm broad × 20 mm high. Please do not use any other dimensions))

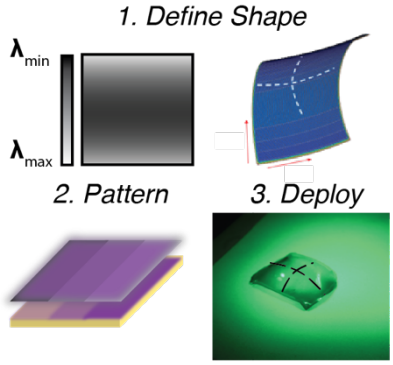

# Supporting Information

**Title** Blueprinting Photothermal Shape-Morphing of Liquid Crystal Elastomers

*Alexa S. Kuenstler, Yuzhen Chen, Phuong Bui, Hyunki Kim, Antonio DeSimone*, Lihua Jin*, and Ryan C. Hayward**

***Constitutive Model of LCEs for FEM Simulations***

We use the commercial software Abaqus/Standard for our finite element simulations. We implemented the following neo-classical free energy density [1] for LCEs in Abaqus by writing a user-defined material subroutine (UMAT)

$$\psi = \frac{\mu}{2}[\mathrm{Tr}(\tilde{\boldsymbol{g}}^{-1}\mathbf{F}\tilde{\boldsymbol{g}}_0\mathbf{F}^{\mathrm{T}}) - 3] + \frac{K}{2}(J-1)^2 - \mu \ln J, \quad \text{(S1)}$$

where $\mu$ is the shear modulus, $K$ is the bulk modulus, $\mathbf{F}$ is the deformation gradient and $J = \det(\mathbf{F})$, $\tilde{\boldsymbol{g}}$ is a temperature-dependent three-dimensional metric tensor that describes the anisotropy of LCEs with respect to the isotropic phase in the current configuration,[2] and $\tilde{\boldsymbol{g}}_0$ denotes $\tilde{\boldsymbol{g}}$ in the reference configuration which is selected as the nematic phase at temperature $T$ = 60℃. The metric tensor $\tilde{\boldsymbol{g}}$ can be expressed as

$$\tilde{\boldsymbol{g}} = \tilde{g}_\perp\left[\mathbf{I} + \left(\frac{\tilde{g}_\parallel}{\tilde{g}_\perp} - 1\right)\boldsymbol{n}\otimes\boldsymbol{n}\right], \boldsymbol{n} = \frac{\mathbf{F}\boldsymbol{n}_0}{|\mathbf{F}\boldsymbol{n}_0|}, \quad \text{(S2)}$$

where $\tilde{g}_\parallel$ and $\tilde{g}_\perp$ are eigenvalues of $\tilde{\boldsymbol{g}}$ parallel and orthogonal to the director and $\tilde{g}_\parallel\tilde{g}_\perp^2 = 1$, $\boldsymbol{I}$ is a 3-by-3 identity matrix, $\boldsymbol{n}$ is a unit vector along the director, and $\boldsymbol{n}_0$ denotes $\boldsymbol{n}$ in the reference configuration. The stretch $\lambda$ relates to the metric tensors by

$$\lambda = \sqrt{\tilde{g}_\parallel/\tilde{g}_{0\parallel}}, \quad \text{(S3)}$$

where $\tilde{g}_{0\parallel}$ is the eigenvalue of $\tilde{\boldsymbol{g}}_0$ parallel to the director. To determine the dependence of $\tilde{g}_\parallel$ and $\tilde{g}_\perp$ on temperature, we fit the stretch-temperature relation to the experimental data (**Figure 1**C) and obtain

$$\lambda = 0.6\sqrt{1 + 1.778\frac{120-T}{60}}, \quad \text{(S4)}$$

where $T$ denotes temperature within the range of 60℃ to 120 ℃. The stretch $\lambda_\perp$ perpendicular to the director (**Figure 1**C) can be calculated based on incompressibility

$$\lambda_\perp = \sqrt{1/\lambda}. \quad \text{(S5)}$$

**Equations** (S4) and (S5) indicate that upon heating, LCEs transition from the nematic phase ($T$ = 60℃) to the isotropic phase ($T$ = 120℃), yielding a contractive stretch of 0.6 and a tensile stretch of 1.29 parallel and orthogonal to the director, respectively. From the definition of the metric tensor, we know that $\tilde{g}_\parallel(T = 120℃) = 1$, and therefore, according to **Equation** (S3), we have $\tilde{g}_{0\parallel} = 1/\lambda^2(T = 120℃)$ = 2.778. Based on **Equations** (S3) and (S4), the dependence of $\tilde{g}_\parallel$ on temperature can be expressed as

$$\tilde{g}_\parallel = 1 + 1.778\frac{120-T}{60}, \quad \text{(S6)}$$

and $\tilde{g}_\perp$ can be obtained by $\tilde{g}_\perp = \sqrt{1/\tilde{g}_\parallel}$.

Self-Shadowing FEM Models

Here we numerically show how self-shadowing effect influences oscillating morphing shown in **Figure** 2D-G. The film with a specific pattern (**Figure** 2D) is illuminated from a 30° angle with respect to the substrate along the edge parallel to the director. Initially, the light intensity is the same everywhere on the film and thus the stretch distributions on photoactive and non-photoactive regions are uniform (**Figure** S5A). The photoactive region curls up, forming Mode 1. Since the angle between the bent photoactive region and the substrate is comparable to 30°, the light can be blocked by the film itself. Therefore, the light intensity in the photoactive region becomes non-uniform: the part around the vertex has a higher light intensity than the part away from the vertex. This non-uniform light intensity leads to non-uniform stretch distributions (**Figure S**5B), yielding a full wavelength wrinkle (Mode 2, **Figure**

**S**5C). Once the Mode 2 is formed, the film itself is unable to block the light. The uniform light intensity is recovered and thus the mode of the film is switched from Mode 2 back to Mode 1.

Stretch Profiles for Given Constant Gaussian Curvature

We obtain the stretch profiles giving constant Gaussian curvature by numerically solving **Equation** (2). The target constant (non-dimensional) Gaussian curvature $Kw^2$ is $\pm 0.8$. **Equation** (2) can be solved using Matlab ODE45 solver with a relative error tolerance of $1\text{x}10^{-10}$. The initial conditions are adjusted such that the stretches are experimentally accessible in our system. To define a stretch profile yielding the same Gaussian curvature as the target one, we fit a 9th-order polynomial to the solution such that the relative error of the obtained Gaussian curvature is less than $1\text{x}10^{-6}$. As a result, the stretch profile corresponding to positive Gaussian curvature 0.8 is

$$\lambda(v) = 0.0008016v^9 - 0.008048v^8 + 0.02585v^7 - 0.05128v^6 + 0.07006v^5 - 0.09382v^4 + 0.1015v^3 - 0.4649v^2 + 0.45v + 0.78, \quad \text{(S7)}$$

and the stretch profile corresponding to negative Gaussian curvature -0.8 is

$$\lambda(v) = -0.0003549v^9 - 0.002021v^8 + 0.01206v^7 - 0.01331v^6 - 0.007834v^5 - 0.00651v^4 + 0.04632v^3 + 0.3555v^2 - 0.4v + 0.9. \quad \text{(S8)}$$

***Analytical Shape Prediction***

We consider a two-dimensional surface $\omega$ in $\mathbb{R}^2$ immersed in a three-dimensional Euclidean space $\mathbf{E}^3$ and predict its three-dimensional (3D) shape produced by the metric tensor shown in **Equation** (1).

The Gaussian curvature $K$ of this surface can be computed by[3]

$$-EK = (\Gamma_{12}^2)_{,u} - (\Gamma_{11}^2)_{,v} + \Gamma_{12}^1\Gamma_{11}^2 + \Gamma_{12}^2\Gamma_{12}^2 - \Gamma_{11}^2\Gamma_{22}^2 - \Gamma_{11}^1\Gamma_{12}^2, \quad \text{(S9)}$$

where $E = g_{11} = \lambda^2$, $(\ )_{,u}$ and $(\ )_{,v}$ are partial derivatives with respect to $u$ and $v$, $\Gamma^{\alpha}_{\beta\gamma}$ $(\alpha, \beta, \gamma = 1, 2)$ are the Christoffel symbols, which equal

$$\Gamma^1_{11} = 0, \Gamma^1_{12} = \Gamma^1_{21} = \lambda'/\lambda, \Gamma^1_{22} = 0, \Gamma^2_{11} = -\lambda^2\lambda', \Gamma^2_{12} = \Gamma^2_{21} = 0, \Gamma^2_{22} = -\frac{1}{2}\lambda'/\lambda. \quad \text{(S10)}$$

Here $(\ )'$ denotes differentiation with respect to $v$. With Equations (S9) and (S10), we can obtain the dependence of Gaussian curvature $K$ on stretch profile $\lambda(v)$, as shown in Equation (2).

We assume that the 3D shape is axisymmetric about the $v$ axis and thus the map $\boldsymbol{\chi}$: $\omega \subset \mathbb{R}^2 \longrightarrow \widehat{\omega} \subset \boldsymbol{E}^3$ is given by

$$\boldsymbol{\chi}(u, v) = \left[ r(v)\cos\left(\frac{u}{R_0} + \psi(v)\right) \quad r(v)\sin\left(\frac{u}{R_0} + \psi(v)\right) \quad z(v) \right], u \in [0, l], v \in [0, w], \quad \text{(S11)}$$

where functions $r$, $\psi$ and $z$ depend only on $v$, and $R_0$ is a positive constant that will be determined later. The metric tensor of the surface $\widehat{\omega}$ is given by

$$\boldsymbol{g}_{\widehat{\omega}} = \boldsymbol{\nabla}\boldsymbol{\chi}^{\mathrm{T}}\boldsymbol{\nabla}\boldsymbol{\chi} = \begin{bmatrix} \left(\frac{r}{R_0}\right)^2 & \frac{r^2\psi'}{R_0} \\ \frac{r^2\psi'}{R_0} & r'^2 + z'^2 + r^2\psi'^2 \end{bmatrix}. \quad \text{(S12)}$$

Since the LCE sheets are very thin, it is reasonable to assume that their final configurations are essentially stress-free and their metric tensors given by **Equation** (S12) match the target metric tensor shown in **Equation** (1), i.e.

$$\begin{bmatrix} \left(\frac{r}{R_0}\right)^2 & \frac{r^2\psi'}{R_0} \\ \frac{r^2\psi'}{R_0} & r'^2 + z'^2 + r^2\psi'^2 \end{bmatrix} = \begin{bmatrix} \lambda(v)^2 & 0 \\ 0 & \frac{1}{\lambda(v)} \end{bmatrix}. \quad \text{(S13)}$$

From **Equation** (S13), we obtain

$$r(v) = \lambda(v)R_0, \quad \text{(S14)}$$

$$\psi'(v) = 0, \quad \text{(S15)}$$

$$z'(v) = \pm\frac{1}{\sqrt{\lambda(v)}}\sqrt{1 - \left(R_0\sqrt{\lambda(v)}\lambda'(v)\right)^2}, R_0 \leq \frac{1}{\sqrt{\lambda(v)}|\lambda'(v)|}. \quad \text{(S16)}$$

Given a stretch profile $\lambda(v)$,we can obtain $r(v)$ from **Equation** (S14) and $z(v)$ by evaluating numerically the integral on the right-hand side of **Equation** (S16). In addition, we set $\psi = 0$. The 3D shape for this stretch profile can then be determined by **Equation** (S11**)** with an appropriate $R_0$, which is selected such that the following bending energy is minimized

$$E_b = \int_0^l \int_0^w (4H^2 - K) du dv, \tag{S17}$$

where $H$ and $K$ denote mean and Gaussian curvatures of the surface $\widehat{\omega}$, respectively.

The prediction of the geometric theory outlined above match closely the results of the FEM simulations, as shown in **Figures** 3, 4, **S**6, **S**8. The fact that isometric embeddings of the target metric with the lowest possible bending energy agree very well with those obtained by numerical simulations indicates that the configurations obtained numerically with FEM (and, by extension, the configurations observed experimentally) obey the target metric almost fully and thus are nearly stretch-free.

Moreover, the good match between the predictions of the geometric theory (which does not rely on the choice of a constitutive model and of material parameters for the material response) and the results of the FEM numerical simulations (which use a specific constitutive model based on the neo-classical free energy density) suggest that the morphing concept we demonstrate is robust, with the potential to be used for other materials beyond those considered in this paper.

***Prescription of Photomasks***

The workflow of determining the appropriate photomask to generate a desired shape is shown in Figure S7. A calibration curve for stretch as a function of % black was generated by performing a linear fit of experimentally-measured stretch. Next, the computed stretch profile is decomposed into 256 slices as a function of v and the calibration curve is used to define a numerical value between 0 (0% black) and 1 (100% black). Finally, the image() and

colormap(gray) functions in Matlab are used to convert the 256 slices into a square image where each slice has a constant gray value along u. Following generation of the grayscale images, masks are re-sized in Illustrator to the appropriate dimensions.

***Thermal and Mechanical Properties***

Thermal gravimetric analysis (TGA) was performed using a TA instruments TGA 2950. Samples were heated from room temperature at 20 °C $min^{-1}$ to 600 °C and the weight percent of gold nanoparticles was calculated from the difference in maximum weight loss between neat and nanocomposite samples. Differential scanning calorimetry (DSC) was performed on a TA instruments DSC Q200. Samples of ≈ 3 mg mass were heated to 150°C, cooled to -50 °C, and heated again to 150°C at 10°C. All values were calculated from the second heating cycle. Mechanical properties were determined from tensile tests performed on 10 mm x 1 mm x 0.05 mm strips using a TA instruments Q800 Dynamic Mechanical Analyzer. Samples were loaded along the director at 0.2 N $min^{-1}$ and the elastic moduli were calculated from linear fits to the initial linear regime of the deformation curve.

***Heat Transfer Calculations***

FEM

The temperature profile within a thin illuminated sheet is simulated using PDE Toolbox in Matlab. The simulated geometry is an axisymmetric disk of material with thermal conductivity $k$ = 0.2 W $m^{-1}$ $K^{-1}$, radius $a_d$ = 5 mm and thickness $t$ = 50 μm, possessing a centered circular photothermal inclusion of radius $a_p$ = 2.5 mm (**Figure S2**). In reality, the heat generation will decrease through the thickness following an exponential, rather than step-wise, function, with a penetration depth that depends on nanoparticle concentration. As a simplified approach to understand the potential effects of this non-uniformity in heat

generation through the thickness, we therefore take the photothermal inclusion to occupy only the top half of the disk thickness. The photothermal heat generation in this region is estimated as $Q = 3.2*10^7$ W m$^{-3}$, chosen to match the total heat generated based on the maximum experimental value of absorbance (A ≈ 0.7) and a light intensity of 200 mW cm$^{-2}$. We treat heat loss from the disk as dominated by convection, with a heat transfer coefficient of $h$ = 33 W m$^{-2}$ K$^{-1}$ as estimated from heat transfer correlations for a horizontal plate.[4] We consider two limits: (i) free convection from both the top and bottom surfaces of the disk and (ii) free convection from only the top surface and insulation at the bottom surface. The experiments are expected to fall between these limits, since convection from the bottom surface is likely to be less efficient than from the top, due to the presence of the underlying hot plate. The results shown in **Figure S2**B-C reveal two key points. First, thermal diffusivity leads to in-plane broadening (**Figure S2**B) by only a modest amount, with the lateral variation in temperature restricted to a region of only ~ 1 mm across the edge of the heated feature. To better understand the extent of lateral broadening, we turn to the approximate 1D analytical solution in the following section. Second, for both cases, the temperature is nearly constant through the thickness of the film (**Figure S2**C), despite the generation of heat only in the top half of the film, due to the small thickness of the heated features in comparison to their lateral dimensions, and the rapid transport of heat by thermal conduction across the film thickness.

**Analytical Model**

As the FEM model results confirm the uniformity of temperature along the z-direction of the plate, we can further reduce the heat transfer problem to 1D, where we balance the divergence in radial flux of heat outward from the heated region against the heat lost by convection, i.e.

$$kt\left[\frac{1}{r}\frac{d}{dr}\left(r\frac{dT}{dr}\right)\right] = hT \qquad \text{(S18)}$$

with the following boundary conditions: (1) $T = T_0$ at $r = a_p$, and (2) $T \to 0$ at $r \to \infty$. Here, $T$ represents the temperature increase above ambient. The appropriate solution to this (Helmholtz) equation, which satisfies the boundary conditions is

$$T = T_0 K_0(qr)/K_0(qa_p) \quad \text{(S19)}$$

where $K_0$ represents the modified Bessel function of the second kind, and $q^{-1} = (kt/h)^{1/2}$ describes the characteristic length-scale for spatial broadening of the temperature profile. Using the parameters $t$ = 0.05 mm, $k$ = 0.2 W m$^{-1}$ K$^{-1}$, and $h$ = 33 W m$^{-2}$ K$^{-1}$ as above, this length is $q^{-1}$ = 0.55 mm, consistent with the limited extent of lateral broadening found via FEM.

**Measurement**

Photothermal heat generation was measured using a FLIR E4 thermal imaging camera (**Figure S3**E). In good agreement with the FEM results, the temperature increase above ambient in the center of the photothermal region was ≈ 20 K, and lateral broadening of the temperature profile, relative to the illuminated region, occurred over a characteristic length scale of ≈ 0.5 mm.

***List of Movies***

1. Top-view of snapping film
2. Side-view of snapping film

Supplementary Figures

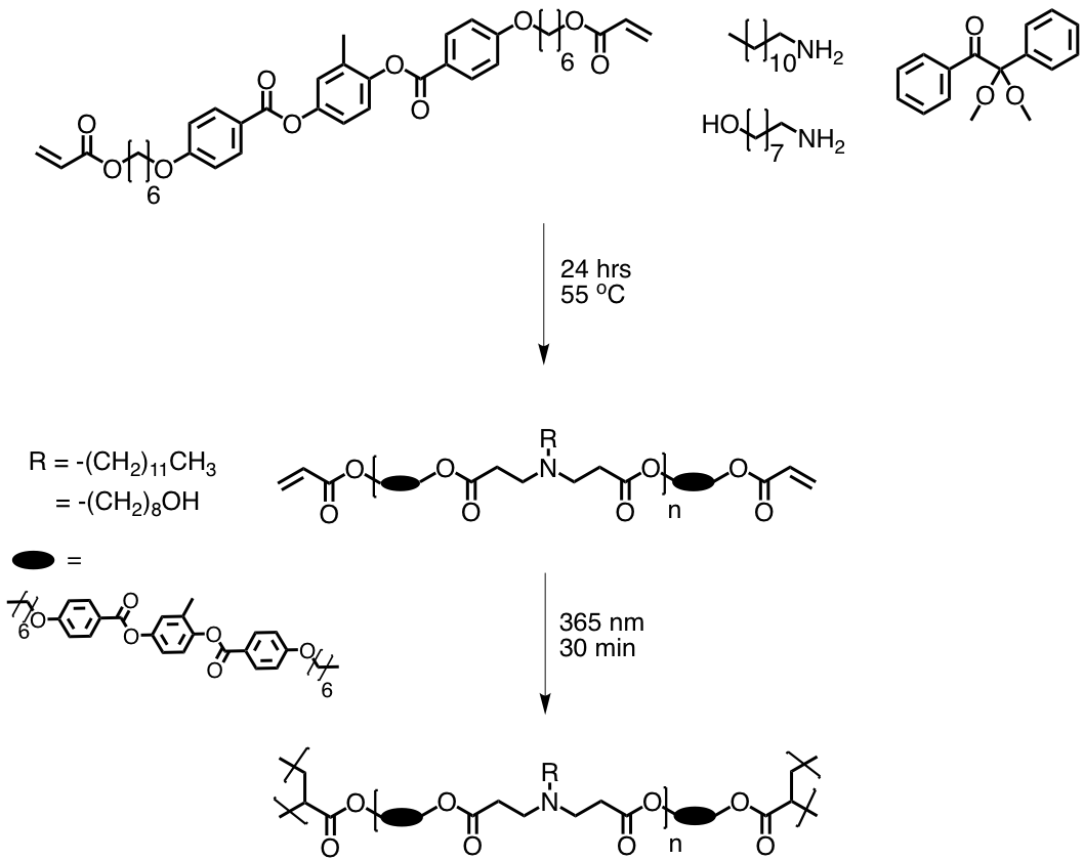


**Scheme S1**. Synthesis of liquid crystal elastomers. Telechelic oligomers are first synthesized via the reaction of a slight excess of diacrylate mesogens to amine chain extenders and the cross-link density is dictated by this stoichiometry. Subsequently, the preserved diacrylate end-groups are used to photo-crosslink the oligomers to lock-in a monodomain alignment.

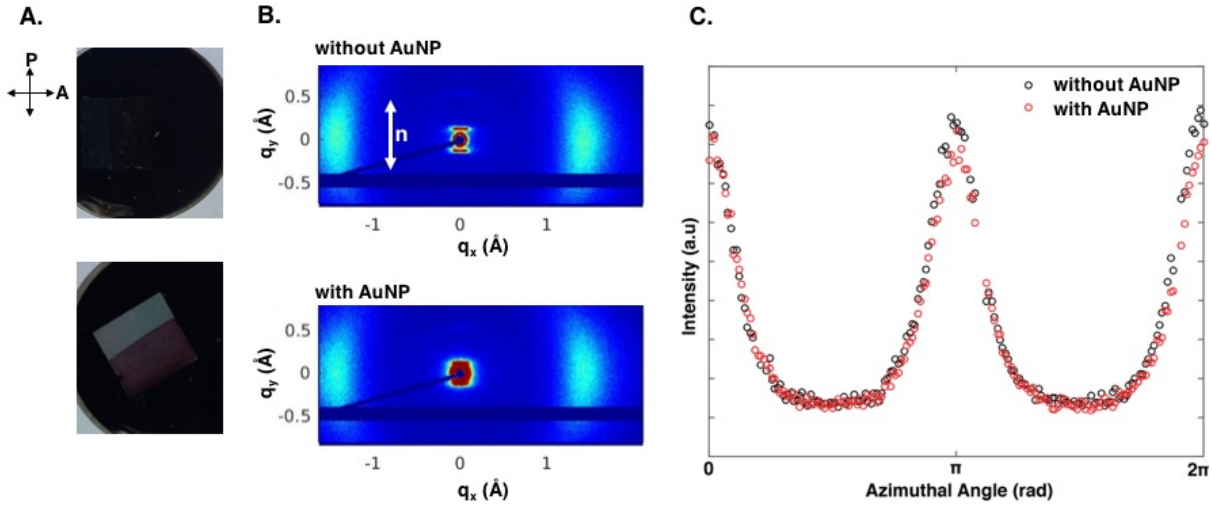


**Figure S1**. **(A)** A patterned LCE viewed through cross-polarizers. The sample is uniformly dark when the director is parallel to the polarizer and bright when the director is at a 45° to the polarizer, indicating a planar nematic sample with a unidirectional director field. **(B)** Wide-angle x-ray scattering of regions of the sample without (top) and with (bottom) AuNPs shows good alignment of mesogens in both cases. **(C)** Average intensity vs azimuth for regions of the same film with and without AuNPs. The order parameter in both regions is S ≈ 0.6.

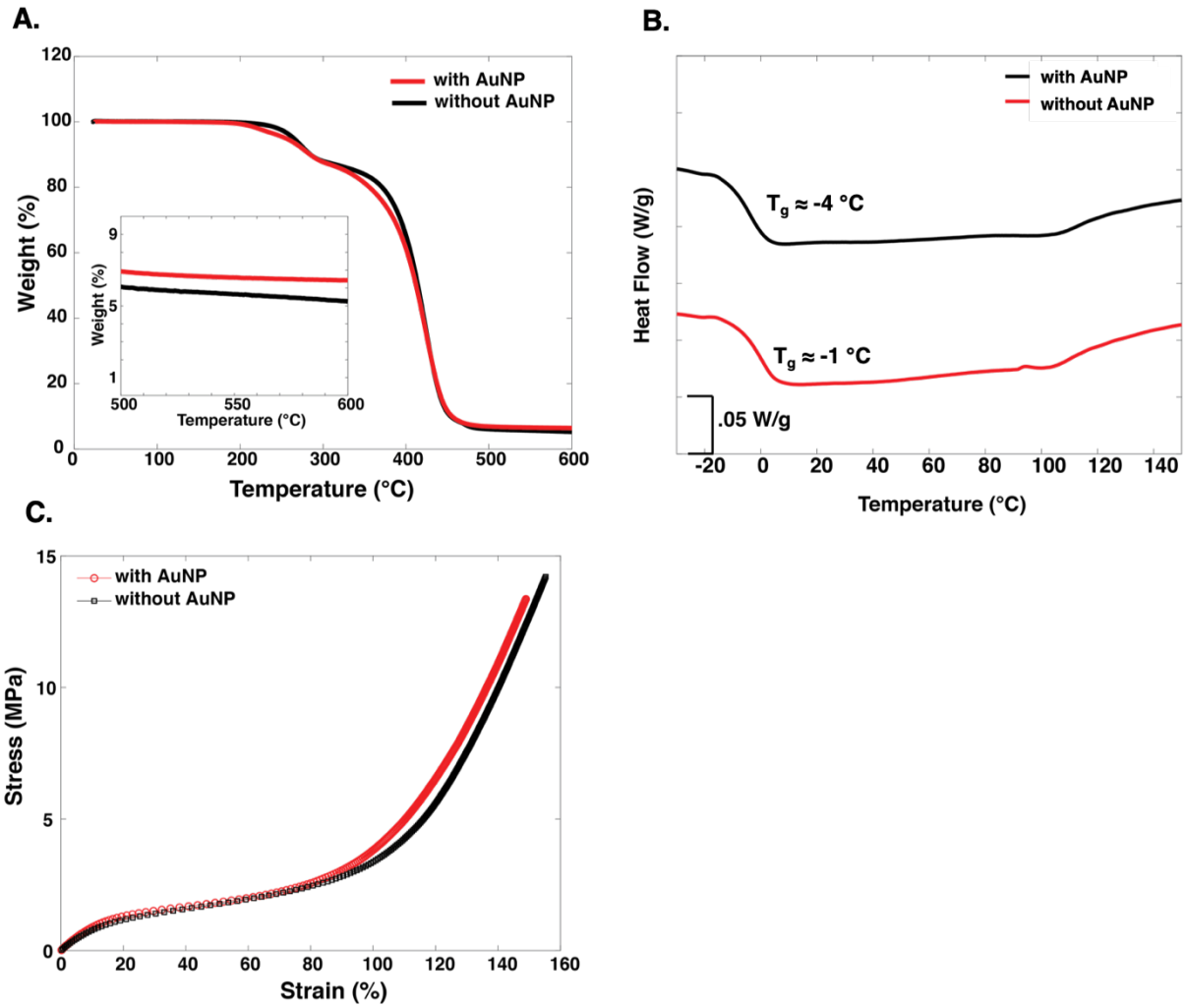


**Figure S2**. **(A)** Nanocomposites contain ≈ 1 wt% nanoparticles as evaluated by thermogravimetric analysis (TGA). **(B)** DSC thermograms of a LCE with and without AuNPs. Glass transition temperatures are within instrumental error indicating that introduction of nanoparticles does not cause significant mechanical changes. An upturn at ≈ 100 °C is indicative of $T_{NI}$, consistent with reports for similar systems where no nematic-isotropic endotherm is observed due to the small magnitude ($\Delta H < 10$ J/g) and the breadth of the transition over a large temperature range. (**C**) Stress versus strain curves show that the modulus remains unchanged after introduction of nanoparticles.

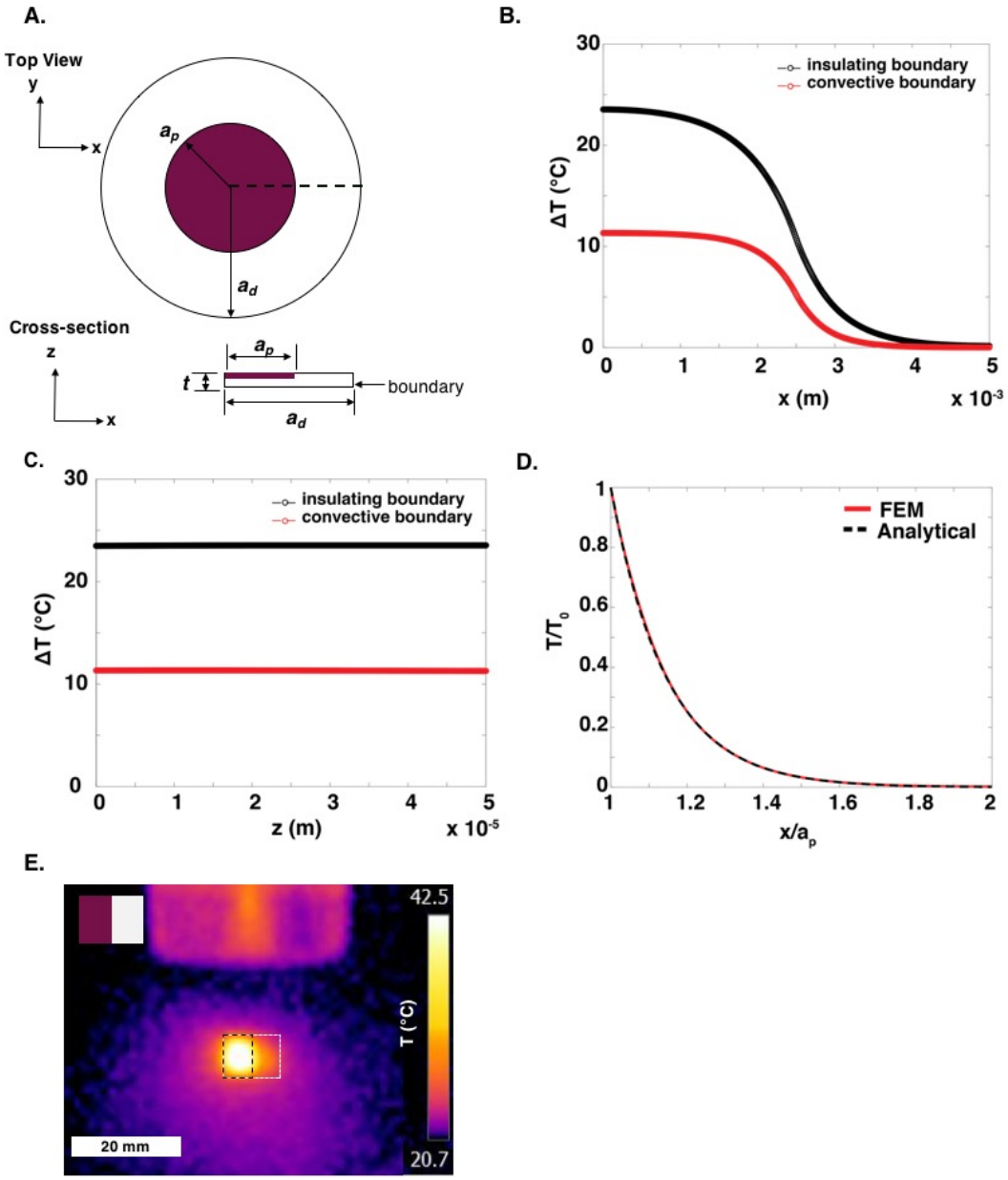


**Figure S3. (A)** Geometry of a photoactive disk in FEM simulations (top) and its cross-section (bottom) for a cut made as indicated by the dashed line. The bottom boundary is subjected to an insulating or a convective boundary condition in separate trials. **(B)** Radial temperature distribution shows limited thermal broadening (< 1 mm) for both boundary conditions. **(C)** Through-thickness temperature variation is minimal (< 0.2 °C) for both boundary conditions. **(D)** Comparison of FEM and analytical solution shows excellent agreement. **(E)** Thermal image of a film (outlined with a white dotted line) containing a photothermal stripe (outlined in a black dashed line) shows heat generation is localized to the nanoparticle-containing region of the film.

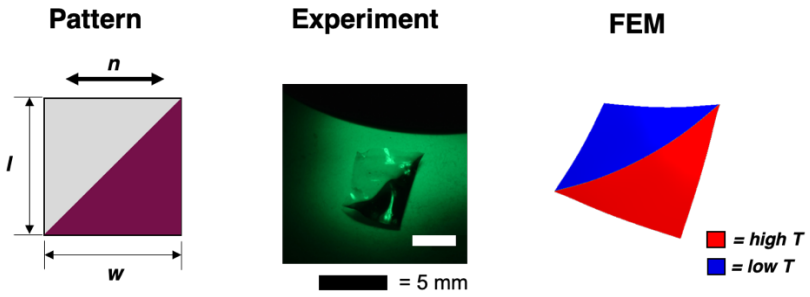


**Figure S4.** Patterned nanocomposite that oscillates under oblique illumination is observed to adopt a stationary morphology under overhead illumination.

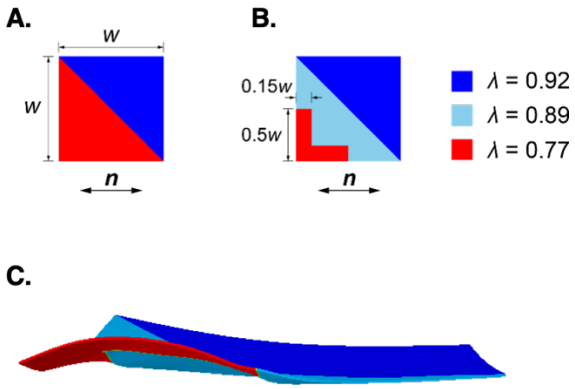


**Figure** S5. (A) The patterned film that leads to oscillation. (B) A simplified model of self-shadowing in FEM simulations is realized by imposing a maximum contraction (red) along the edge closest to the light source and a smaller contraction in regions that would be blocked by the light (light blue). (C) This model produces Mode 2 buckling, suggesting that self-shadowing can shift the preferred configuration, thereby driving oscillatory snapping.

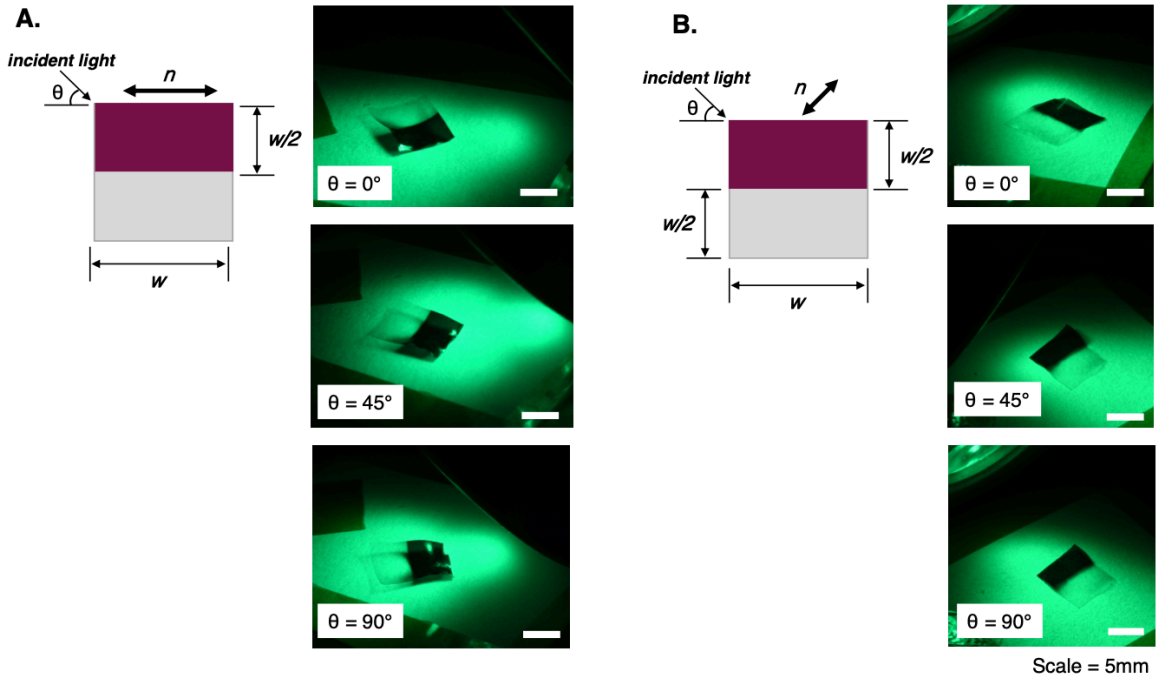


**Figure S6**. Oblique illumination at different angles for a photothermal stripe patterned **(A)** parallel to the director and **(B)** at a 45° to the director. No oscillation is observed for either case regardless of illumination angle.

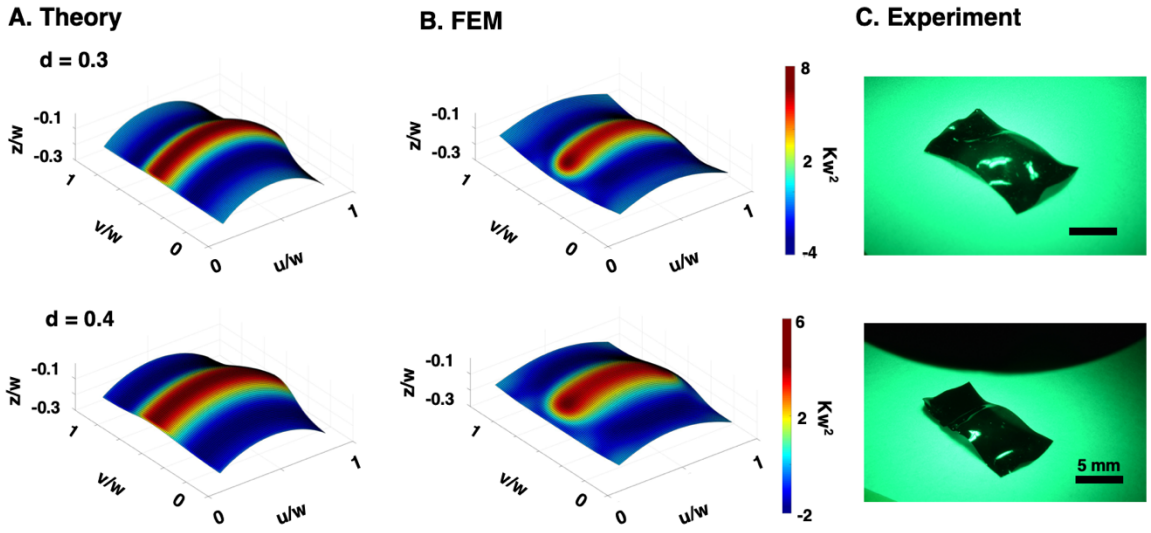


**Figure S7**. Shape predicted by **(A)** Theory and **(B)** FEM for Gaussian stretch profiles with $d$ = 0.3 (top row) and $d$ = 0.4 (bottom row). **(C)** Experiments match the predicted shape.

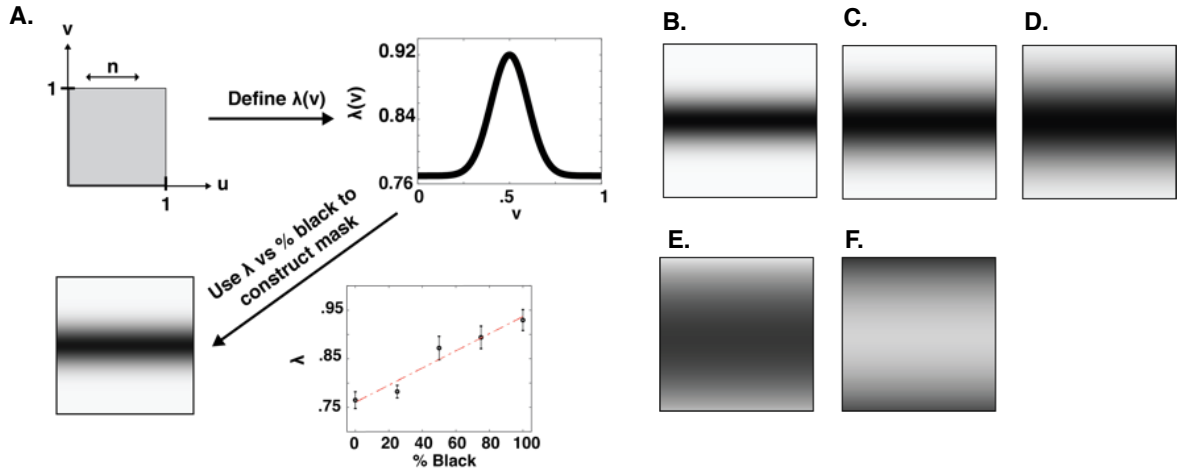


**Figure S8. (A)** Workflow of photomask generation. Photomasks used to pattern Gaussian profiles with **(B)** $d = 0.2$, **(C)** $d = 0.3$, and **(D)** $d = 0.4$ and constant **(E)** positive and **(F)** negative Gaussian curvature.

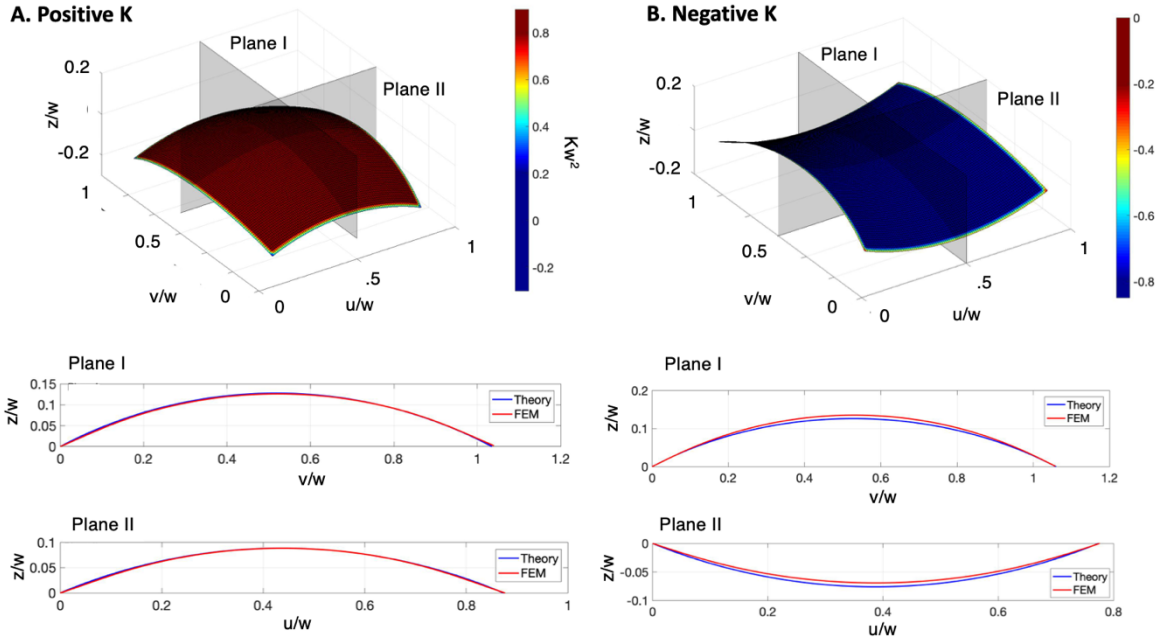


**Figure S9**. Comparison of curvature predicted by theory and FEM for **(A)** positive Gaussian curvature and **(B)** negative Gaussian curvature.

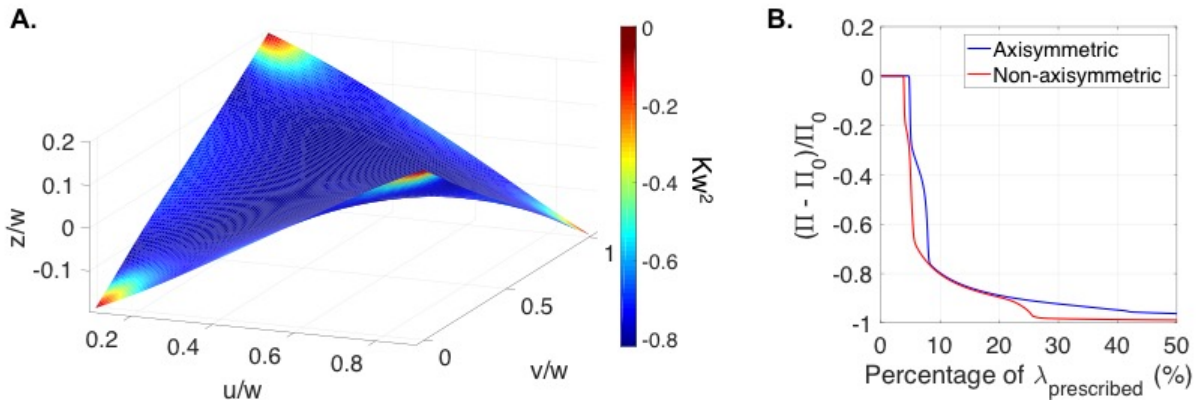


**Figure S10**. **(A)** Non-axisymmetric mode predicted by the FEM for the prescribed constant negative Gaussian curvature via the stretch profile shown in Figure 4A. **(B)** Normalized free energy difference between the curved states Π and the flat state $\Pi_0$ as a function of percentage of prescribed stretches $\lambda_{prescribed}$. The non-axisymmetric mode bifurcates from the flat state at a lower stretch and is energetically preferred. To achieve the axisymmetric mode in the FEM simulations, a symmetric boundary condition about $u/w = 0.5$ is applied. The non-axisymmetric mode, however, has free boundary conditions in the FEM simulations.

***References***

[1] P. Bladon, M. Terentjev, M. Warner, *Phys. Rev. E* **1993**, *47*, 3838.

[2] L. Jin, Z. Zeng, Y. Huo, *J. Mech. Phys. Solids* **2010**, *58*, 1907.

[3] Do Carmo, Manfredo P. Differential geometry of curves and surfaces: revised and updated second edition. Courier Dover Publications, 2016.

[4] J.R. Welty, C.E. Wicks, R.E. Wilson, G.L. Rorrer. *Fundamentals of Momentum, Heat, and Mass Transfer*, John Wiley & Son, Inc, Hoboken, 2008.